The magnetic states of R^{3+} in R_2NiO_4 ($R = Pr, Nd$)

1997 J. Phys.: Condens. Matter 9 2275

(http://iopscience.iop.org/0953-8984/9/10/015)

J. Phys.: Condens. Matter **9** (1997) 2275–2294. Printed in the UK PII: S0953-8984(97)77214-X

The magnetic states of R^{3+} in R_2NiO_4 (R = Pr, Nd)

A T Boothroyd†, A Longmore†, M Castro‡, R Burriel‡ and R S Eccleston§

† Department of Physics, Clarendon Laboratory, University of Oxford, Parks Road, Oxford OX1 3PU, UK

‡ Instituto de Ciencia de Materiales de Aragón, CSIC–Universidad de Zaragoza, 50009 Zaragoza, Spain

§ ISIS Science Division, Rutherford Appleton Laboratory, Chilton, Didcot, Oxon OX11 0QX, UK

Received 16 August 1996, in final form 20 November 1996

Abstract. We have investigated the compounds Pr_2NiO_4 and Nd_2NiO_4 with the aim of establishing the magnetic energy levels and wavefunctions of the Pr^{3+} and Nd^{3+} ions. We report neutron inelastic scattering, specific heat capacity and susceptibility measurements, and analyse the data in two stages to obtain a model for the crystal field acting on the Pr^{3+} and Nd^{3+} ions. First we find the best model for the crystal field assuming tetragonal symmetry, and then we refine this model to include terms describing the actual monoclinic site symmetry *m* (C_{1h}). By this process we obtain a good description of the available data. We find that the low-temperature magnetic properties of Pr^{3+} in Pr_2NiO_4 are dominated by two singlets, separated in energy by 4.3 meV. The Nd^{3+} level scheme consists of five, roughly equally spaced doublets, the ground and first excited states separated by 7.1 meV. The doublets are split by an effective magnetic field from the ordered Ni^{2+} moments, and the size of the splitting of the ground-state doublet is 1.5 meV.

1. Introduction

The stoichiometric R_2NiO_4 (R = La, Pr, Nd) compounds are layered perovskites which are similar in many respects to their cuprate cousins, R_2CuO_4. Like the cuprates, the nickelates display a rich variety of structural and magnetic phases [1–4], and the transport properties vary greatly if the materials are doped with holes or electrons [5, 6].

Of central importance in these materials is the occurrence of antiferromagnetism on the transition metal–oxygen planes at temperatures below approximately 325 K [1–3]. In the nickelate compounds containing Pr and Nd a whole sequence of magnetic structures, involving both the lanthanide and transition metal ions, have been observed and characterized in some detail [1, 2]. This complex magnetic behaviour is a consequence of the interplay between localized 4f moments and the antiferromagnetically correlated NiO_2 planes, which in doped compounds can give rise to other interesting phenomena. In doped cuprates, for example, superconductivity [7] and a proposed new heavy-fermion state [8] have been discovered.

Any microscopic theory of these effects will require the electronic states of the ions involved. In the case of the R^{3+} ions, the $4f^n$ configuration is split by the local crystalline electric field (CEF) into a series of energy levels, the nature of which determines the magnetic properties at any given temperature. The aim of this paper is to establish as closely as possible the energy levels and corresponding wavefunctions for the R^{3+} ions in

0953-8984/97/102275+20$19.50

stoichiometric Pr_2NiO_4 and Nd_2NiO_4. Information from neutron scattering and heat capacity measurements is used to refine a common model for the crystal field in both compounds, and the results are checked for consistency against the magnetic susceptibility. We undertook a similar task for Pr_2CuO_4 and Nd_2CuO_4 several years ago [9, 10], and we will comment on the differences between the two systems.

2. Experimental measurements

2.1. Sample preparation

Polycrystalline samples of stoichiometric R_2NiO_4 (R = Pr, Nd) were prepared by solid-state reaction of R_2O_3 and NiO, followed by reduction. For one batch of Nd_2NiO_4 (used in the inelastic neutron scattering experiments) the initial reaction temperature was 1200 °C and the subsequent anneal was carried out in H_2 gas at 310 °C for several days. The other batches of R_2NiO_4 were reacted at 1350 °C and reduced at 310 °C for 12 h. The samples were reground several times during the reaction to ensure homogeneity. The final products were brown powders, and the phase purity and stoichiometry of selected batches were checked by x-ray diffraction and iodometric titration.

2.2. Neutron inelastic scattering

Neutron inelastic scattering can be used to measure transitions between a set of single-ion, crystal-field eigenstates. The scattering intensity is described by the double-differential cross-section which, in the dipole approximation, can be written as [11]

$$\frac{\mathrm{d}^2\sigma}{\mathrm{d}\Omega\ \mathrm{d}(\hbar\omega)} = \left(\frac{\gamma r_0}{2}\right)^2 F^2(\boldsymbol{Q}) \exp(-2W) \frac{k_f}{k_i} S(\boldsymbol{Q}, \omega) \tag{1}$$

where γ is the gyromagnetic ratio (=1.91), r_0 is the classical electron radius ($=2.82 \times 10^{-15}$ m), $\boldsymbol{Q}$ is the scattering vector, $\hbar\omega$ is the energy transfer, $F(\boldsymbol{Q})$ is the magnetic form factor, $\exp(-2W)$ is the Debye–Waller factor (which is approximately unity at the small Q-values and low temperatures used in the experiments), and k_i and k_f are the magnitudes of the incident and scattered neutron wavevectors. $S(\boldsymbol{Q}, \omega)$ is the response function. If the sample is polycrystalline, and the ions non-interacting, then $S(\boldsymbol{Q}, \omega)$ is independent of $\boldsymbol{Q}$, and consists of a sequence of sharp peaks centred at the transition energies:

$$S(\boldsymbol{Q}, \omega) = \frac{2}{3} \sum_{ij} \rho_i |\langle j|\hat{\boldsymbol{\mu}}|i\rangle|^2 \delta(E_i - E_j - \hbar\omega). \tag{2}$$

In equation (2), $|i\rangle$ and $|j\rangle$ are the initial and final eigenfunctions of the system corresponding to the eigenvalues E_i and E_j, $\hat{\boldsymbol{\mu}}$ is the magnetic moment operator, and ρ_i is the thermal population factor of the initial state.

All of the neutron data were obtained on the time-of-flight spectrometer HET (High Energy Transfer) at the ISIS spallation neutron source [12]. On HET the scattered neutrons are recorded as a function of their flight times in banks of counters positioned regularly about the axis of the instrument. The scattering from the R^{3+} ions was isotropic, and so the intensity was summed azimuthally to yield a series of spectra varying with the scattering angle, ϕ. The detectors in the low-angle bank, with scattering angles in the range $3^\circ \leqslant \phi \leqslant 7^\circ$ ($\langle\phi\rangle = 5^\circ$), are situated at 4 m from the sample and give the best energy resolution. The next set of detectors are 2.5 m from the sample, and cover the angular range 9° to 29°. Finally, there are two banks of detectors at large scattering angles, one at 4 m from the sample with $\langle\phi\rangle = 115^\circ$, and the other at 2.5 m with $\langle\phi\rangle = 133^\circ$.

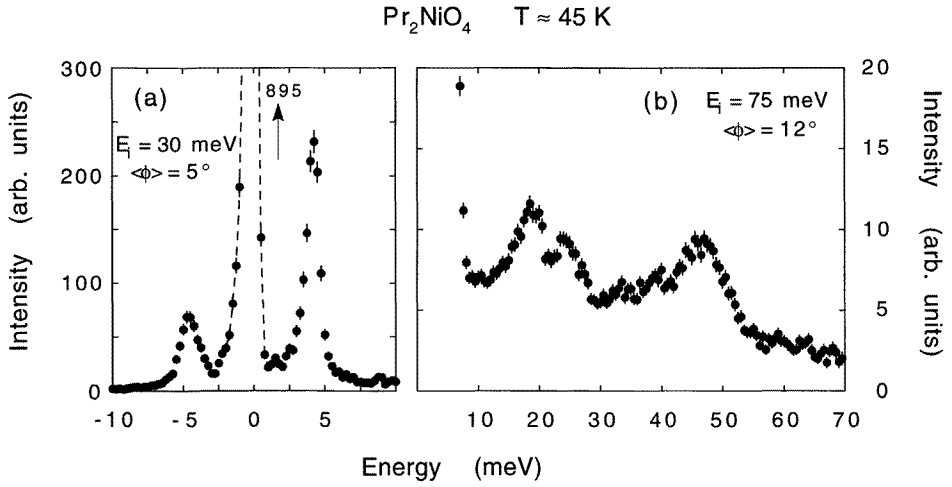

Figure 1. The inelastic neutron scattering spectrum of Pr_2NiO_4 measured on HET at a temperature of 45 K. The data shown in (a) and (b) were measured in different detectors and with different neutron incident energies: (a) the low-angle 4 m detector bank, $E_i = 30$ meV; (b) the inside quarter of the low-angle 2.5 m bank, $E_i = 75$ meV. $\langle\phi\rangle$ is the average scattering angle for the detectors.

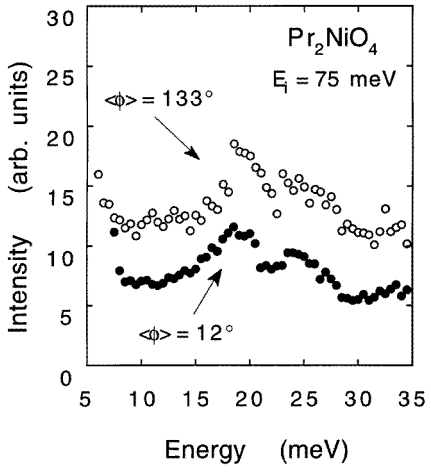

Figure 2. The scattering observed in the low-angle and high-angle 2.5 m detector banks with the same incident energy of 75 meV. This comparison shows that the peaks at 18 meV and 23 meV are not magnetic in origin, and it is likely that they are due to scattering from optic phonons.

The samples of polycrystalline Pr_2NiO_4 and Nd_2NiO_4 used in the neutron experiments were of mass 35 g and 50 g respectively. Measurements were made at temperatures of approximately 45 K (Pr_2NiO_4) and 2 K (Nd_2NiO_4).

The energy spectra presented here have been obtained from the raw time-of-flight data by a transformation which includes a correction for the time-independent background, the detector efficiency and the k_f/k_i term in the neutron cross-section (see equation (1)). Energy

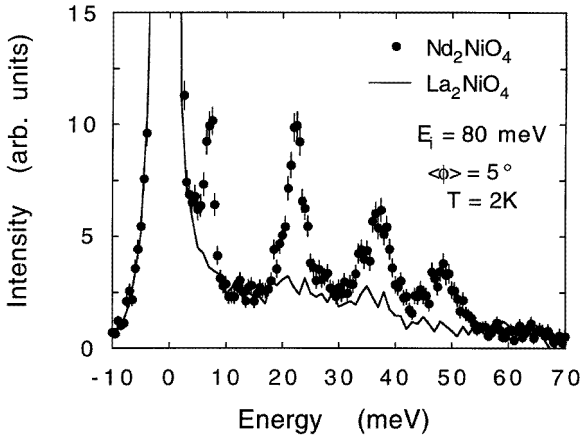

Figure 3. The inelastic neutron scattering from Nd_2NiO_4 showing the four ground-state crystal-field transitions of Nd^{3+}. The data were measured on HET at a temperature of 2 K with neutrons of incident energy 80 meV. The spectrum of La_2NiO_4 is also shown as an indication of the non-magnetic scattering.

spectra of Pr_2NiO_4 and Nd_2NiO_4 are illustrated in figures 1, 2 and 3 (the last has been published previously [13]). Figure 1(a) shows the low-energy part of the spectrum of Pr_2NiO_4 measured in the low-angle, 4 m detector bank with neutrons of incident energy 30 meV. As well as the elastic scattering there are two intense inelastic peaks, centred at -4.3 meV and 4.3 meV, which correspond to the same CEF transition measured in neutron energy gain and energy loss, respectively. Both these peaks, and the elastic peak, have widths that are limited by the instrumental resolution, and the absence of any other peaks at low energies suggests that this CEF transition is from the ground state to the first excited state.

In figure 1(b) we show details of the energy spectrum of Pr_2NiO_4 in the range 10 meV to 70 meV. These data were recorded by the innermost detectors ($\langle\phi\rangle = 12^\circ$) of the low-angle, 2.5 m bank, with neutrons of incident energy 75 meV. There are peaks at approximately 18 meV and 23 meV, and a broader feature extending from 30 meV to 55 meV with a maximum at 47 meV. The 18 meV and 23 meV peaks have the appearance of CEF excitations, but we believe most of the intensity in these peaks is actually from optic phonons. The evidence for this assertion is given in figure 2, which shows that the same two peaks are present in the spectrum measured in the high-angle, 2.5 m bank. The Pr^{3+} magnetic form factor is too small at this angle to allow magnetic scattering to be observed ($|\boldsymbol{Q}| \approx 10$ Å^{-1} at $\phi = 133^\circ$), and so the 18 meV and 23 meV peaks in the high-angle detectors are definitely from phonons. The appearance of these peaks at low angles is due to multiple scattering (one-phonon, one-Bragg-scattering processes). The intensity between 30 meV and 55 meV, on the other hand, was not present in the high-angle detectors, and so we take it to be from magnetic excitations of Pr^{3+}. Because this scattering is broad, whereas the CEF excitations are sharp (cf. figure 1(a)), we conclude that this feature must comprise a number of overlapping CEF peaks originating from transitions connecting both the ground state and the first excited state at 4.3 meV to higher levels.

The energy spectrum of Nd_2NiO_4, shown in figure 3 from a run with incident energy 80 meV, is more straightforward. It consists of four, nearly equally spaced peaks of comparable intensity. We can assign these peaks to CEF excitations of Nd^{3+} because

they are absent both from the high-angle banks and also from the spectrum of an identically constructed sample of La_2NiO_4 measured under the same conditions (shown in figure 3). We expect the La_2NiO_4 spectrum to be a good approximation to the non-magnetic scattering from Nd_2NiO_4.

2.3. Specific heat capacity

AC heat capacity measurements were made in a Sinku Riko ACC-1VL calorimeter which has been modified to permit measurements down to 1.8 K and to improve the accuracy at low temperatures. A slab-shaped sample of pressed powder was used, with a mass of ∼3 mg and a thickness of 0.3 mm. The heating source was a light beam chopped at a frequency of 1 Hz. The temperature was scanned at a rate of 30 K h^{-1}, except at low temperatures when the rate was reduced to 10 K h^{-1}. Absolute values were obtained by scaling the relative values to the heat capacity measured by adiabatic calorimetry above 80 K for Nd_2NiO_4 and above 35 K for Pr_2NiO_4 [14].

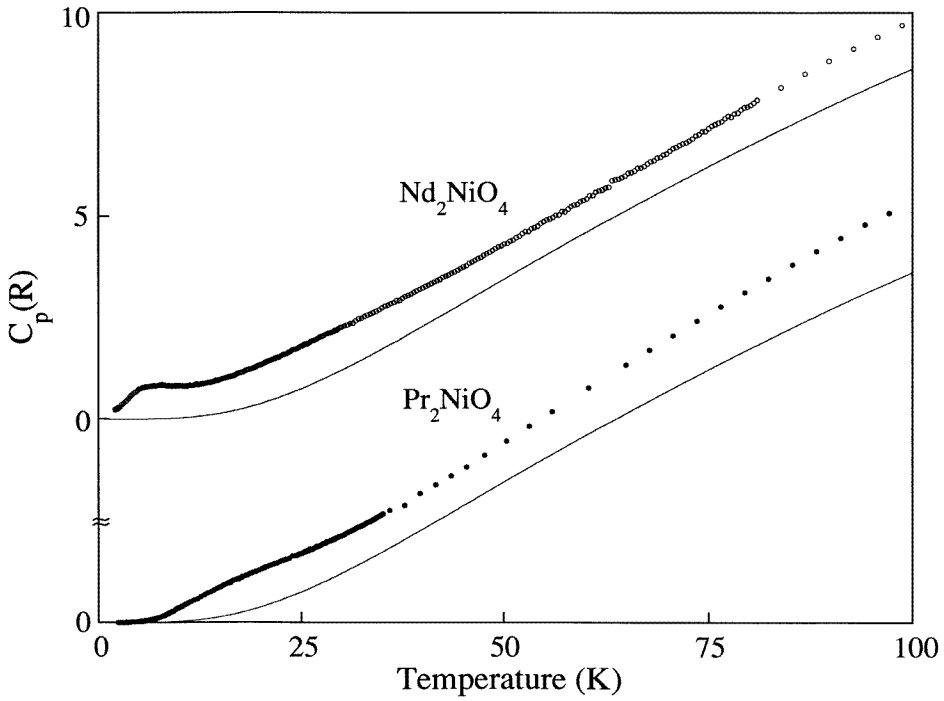

Figure 4. The total molar heat capacities of Pr_2NiO_4 and Nd_2NiO_4. The points are the measurements, and the lines are the calculated lattice contributions based on the measured phonon density of states of La_2NiO_4 [15].

The molar heat capacity measurements are shown in figure 4, together with the lattice contribution calculated from the phonon density of states deduced from inelastic neutron scattering spectra of La_2NiO_4 [15]. Figures 5 show the excess heat capacity ΔC_p, i.e. the difference between the measured heat capacity of R_2NiO_4 and the calculated lattice heat capacity. The curves show anomalies which we will discuss later with reference to the R^{3+} energy levels.

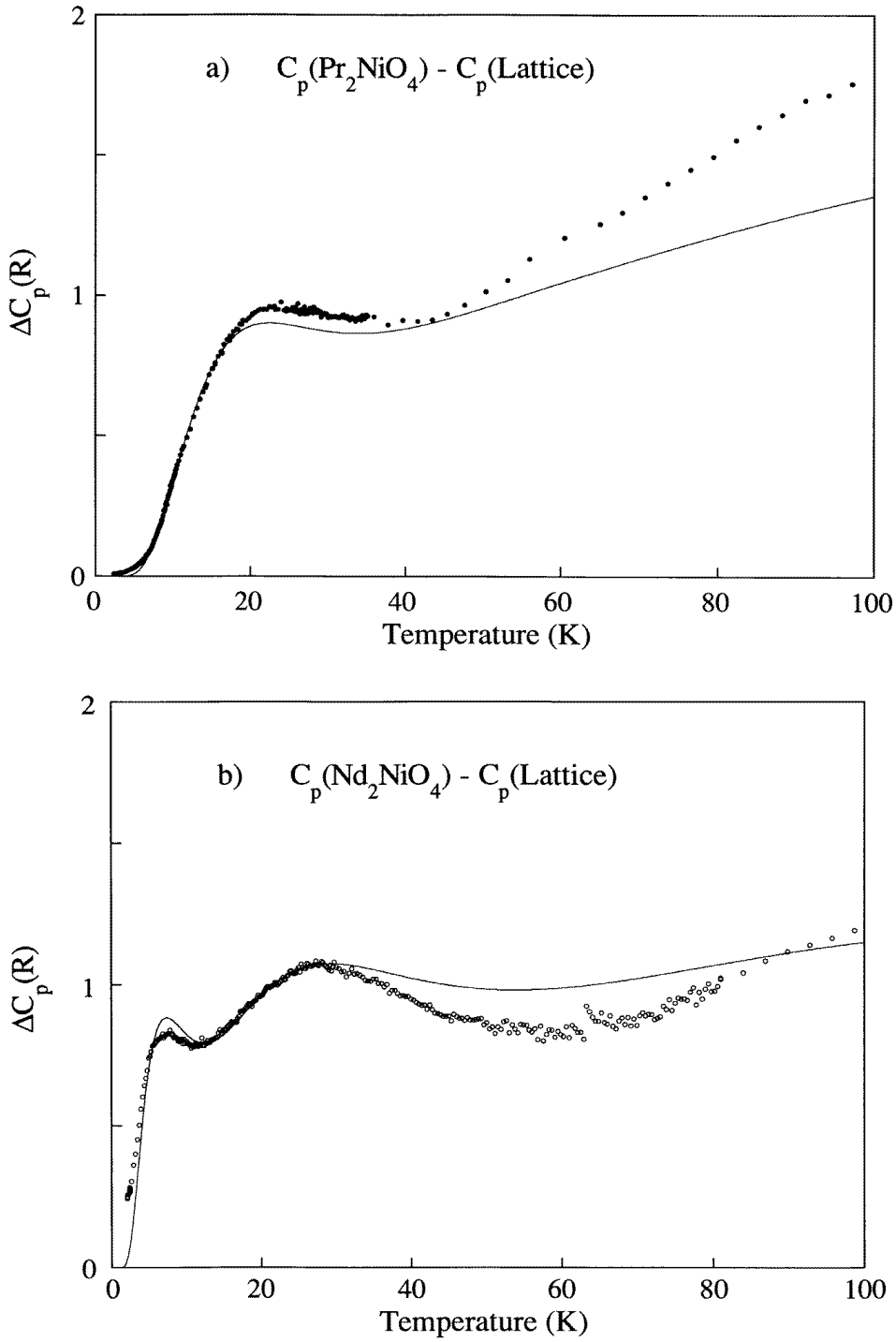

Figure 5. The R^{3+} contribution to the heat capacities. The points are obtained from the data in figure 4 by subtraction of the estimated lattice heat capacity. The curves are the Schottky contribution calculated from the observed energy levels listed in table 2—see later.

2.4. Susceptibility

Ac and dc susceptibility measurements were made in the temperature range 5 K to 300 K with a Quantum Design SQUID magnetometer. The instrument is calibrated regularly, and the absolute accuracy is better than 1%. Samples of mass 300 mg were used. The excitation field for the ac measurement had an amplitude and frequency of 3.5 Oe and 20 Hz respectively.

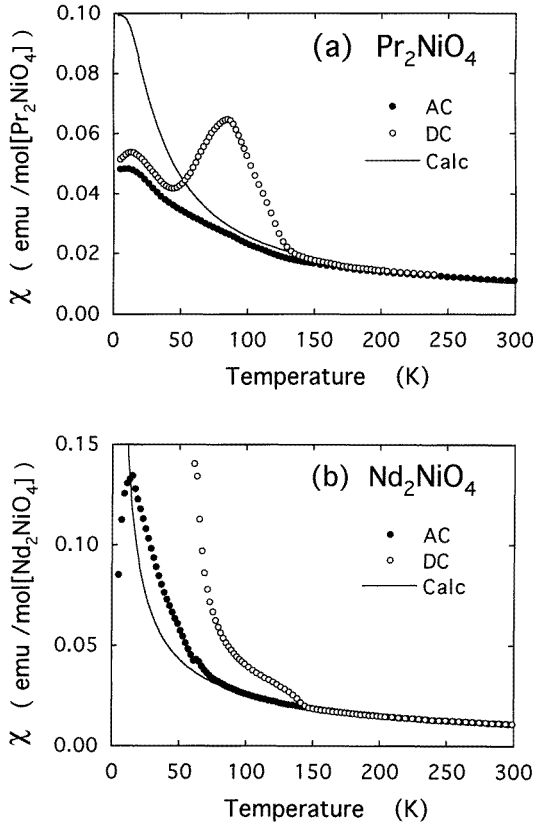

Figure 6. Weak-field ac and dc powder susceptibilities of (a) Pr_2NiO_4 and (b) Nd_2NiO_4. The ferromagnetic impurity contribution and the small contribution to the measured susceptibilities arising from the antiferromagnetically ordered NiO_2 planes have been subtracted from the data. The points are the measured data, and the lines are calculated from the crystal-field model given in table 3—see later.

The measurements were initially made in weak fields, but the ac and dc susceptibilities at room temperature were not consistent with one another, a problem also to be found with results in the literature [16–18]. The source of the problem appears to be impurities, possibly Ni, since our measurements of the room temperature magnetization as a function of applied field revealed a sharp change in slope between 0.2 T and 0.4 T, most likely due to the saturation of a ferromagnetic impurity. The excess low-field susceptibilities saturate below 0.4 T to a saturation magnetization of 0.05 emu g^{-1} for Pr_2NiO_4 and 0.01 emu g^{-1} for Nd_2NiO_4, which in both cases would correspond to an amount of metallic Ni smaller than 0.01% of the sample weight. The results displayed in figures 6 show our weak-field

data corrected for the change in slope in the $M(H)$ curve. A constant susceptibility of 7×10^{-4} emu mol^{-1} has been subtracted from the data to correct for the susceptibility of the antiferromagnetically ordered Ni^{2+} sublattice [4]. This constant susceptibility is consistent with the value (6.75×10^{-4} emu mol^{-1}) which we have calculated for an $S = 1$, square planar, Heisenberg antiferromagnet using the exchange constant $J = -220$ K [17]. Above 150 K the ac and dc curves agree, as should be expected.

The main features of the susceptibilities are similar to those in previous measurements [16–18]. The data show paramagnetic behaviour at high temperature, with an abrupt change in the dc susceptibility at the structural phase transition [2] (at ∼125 K for Pr_2NiO_4 and ∼140 K for Nd_2NiO_4), below which the dc measurements considerably exceed the ac measurements because of canted antiferromagnetism in the Ni^{2+} sublattice in the low-temperature phase. The anomalies at 88 K and 63 K respectively for Pr_2NiO_4 and Nd_2NiO_4 coincide with reorientations in the magnetic structure of the Ni^{2+} sublattice [16, 17]. The rounded maximum at ∼10 K in the ac susceptibility of Nd_2NiO_4 can be attributed to the splitting of the ground-state doublet of Nd^{3+} [14].

3. The crystal-field calculation

The models for the atomic wavefunctions of R^{3+} and for the crystal-field interaction are the same as used in the analysis of the crystal-field excitations in the cuprates, $(Nd, Pr)_2CuO_4$ [10] and $PrBa_2Cu_3O_7$ [19]. The CEF is described by the Hamiltonian

$$H_{CEF} = \sum_{k=2}^{6} B_0^k C_0^k + \sum_{k=2}^{6} \sum_{q=1}^{k} [B^{(c)k}_q (C^k_{-q} + (-1)^q C^k_q) + \mathrm{i} B^{(s)k}_q (-C^k_{-q} + (-1)^q C^k_q)] \qquad k \text{ even} \tag{3}$$

where C_q^k is the qth component of a spherical tensor of rank k related to the normalized spherical harmonic Y_{kq} by $C_q^k = [4\pi/(2k+1)]^{1/2} Y_{kq}$, and the B_q^k are the crystal-field parameters, with the superscripts (c) and (s) indicating the real and imaginary terms for $q > 0$.

To a first approximation, the B_q^k can be expressed as products of two factors:

$$B_q^k = \langle r^k \rangle A_q^k \tag{4}$$

of which the first is the kth moment of the 4f radial wavefunction, and the A_q^k are intrinsic crystal-field parameters, independent of the particular lanthanide ion. In this way it is possible to predict the CEF spectra of different lanthanide ions from a single set of crystal-field parameters. Conversely, we can refine a single set of parameters by fitting to the experimental data for two or more lanthanide ions simultaneously. Parameter scaling was found to work extremely well with the compounds Pr_2CuO_4 and Nd_2CuO_4 [10].

The basis states within which the Hamiltonian equation (3) is diagonalized are the intermediate-coupling atomic wavefunctions obtained by Carnall *et al* [20], which are multiplets of well-defined total angular momentum, J. These multiplets contain $2J + 1$ energy levels whose degeneracies are raised by the crystal-field interaction. The wavefunction of the lowest such J-multiplet is approximately the same as the ground state obtained by applying Hund's rules. The crystal field also mixes wavefunctions from different J-multiplets. In our diagonalizations we used all 13 J-multiplets of Pr^{3+}, but included only the first 11 multiplets of Nd^{3+} (extending 2.2 eV above the ground state) because the complete set was too large to handle computationally. The use of such a detailed atomic

model might at first seem excessive, but is necessary if the same set of intrinsic crystal-field parameters are to be used for both Pr^{3+} and Nd^{3+}, as demonstrated in reference [10].

In addition to the crystal-field Hamiltonian (3) we also included, where appropriate, a molecular-field interaction of the form

$$H_{mf} = -\mu_B \hat{\boldsymbol{\mu}} \cdot \boldsymbol{B}_{mf} \tag{5}$$

where $\hat{\boldsymbol{\mu}}$ is the magnetic moment operator and μ_B is the Bohr magneton. H_{mf} is the energy of the lanthanide ion in an effective molecular field $\boldsymbol{B}_{mf}$ which represents the exchange couplings to the lanthanide and Ni sublattices.

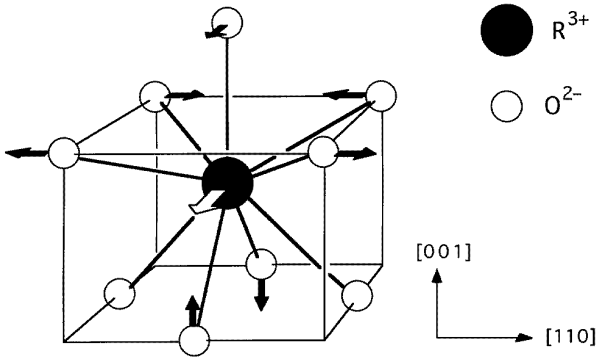

Figure 7. The distribution of nearest-neighbour oxygen ions around the R^{3+} site in the undistorted point group 4*mm*, which is an approximation to the local environment in R_2NiO_4. The arrows indicate the shifts in atomic positions that lead to the actual distorted symmetry *m*.

4. The point charge model

The crystal structure of R_2NiO_4 is orthorhombic at room temperature, but undergoes an orthorhombic-to-tetragonal transition at a temperature T_{c1} in the vicinity of 100 K (T_{c1} = 80 K [3], 115–121 K [2, 14] and 130–138 K [1, 14] for R = La, Pr and Nd respectively). To a first approximation, the symmetry of the R^{3+} site belongs to the tetragonal point group 4*mm* (C_{4v}), as in La_2CuO_4, but because of tilting of the Ni–O octahedra the actual site symmetry is lowered to the monoclinic point group *m* (C_{1h}) in both the orthorhombic and tetragonal phases. Figure 7 shows the distribution of nearest-neighbour oxygen ions around the R^{3+} site in the undistorted point group 4*mm*, and illustrates the shifts in atomic positions that lead to the distorted symmetry *m*.

To describe completely a crystal field with point symmetry *m* requires a total of 14 independent crystal-field parameters [21]. The higher-symmetry, tetragonal point group 4*mm* requires only five parameters. For this reason we began by exploring the attractive possibility that a crystal-field model with symmetry 4*mm* might provide a good starting point from which to derive the actual crystal field.

Assuming that the CEF at the lanthanide site is dominated by the nine nearest-neighbour oxygen ions we used the point charge model [22] to calculate the CEF parameters, and hence the energy spectra, for local environments both with and without the monoclinic distortion. From the extent of the changes induced by the distortion we could then assess whether it was reasonable to try to find an approximate description of the CEF in tetragonal symmetry. We emphasize that the point charge model is only expected to provide useful information

Table 1. Coordination factors[a] (in units of $\text{Å}^{-(k+1)}$) from the point charge model calculations for (a) Pr_2NiO_4 and (b) Nd_2NiO_4. Values are calculated for the approximate, undistorted local structure (point group $4mm$ (C_{4v})), and for the actual, distorted structure (point group m (C_{1h})). For the undistorted structure the coordination factors are given with respect to two different sets of axes, firstly with the CEF axes parallel to the crystallographic axes, and second with the CEF z-axis parallel to [110] and the CEF x-axis parallel to $[00\bar{1}]$. For the distorted structure, only the latter axes were used. The inter-ionic distances used to calculate the γ_{kq} were obtained from the refined crystal structures given by Fernández-Díaz *et al* [2], and Rodríguez-Carvajal *et al* [1]. Complex coordination factors are given in brackets as $({\gamma^{(c)}}_{kq}, {\gamma^{(s)}}_{kq})$. Otherwise the factor is real, and the value given is ${\gamma^{(c)}}_{kq}$.

		Undistorted ($4mm$)		Distorted (m)
k	q	CEF z-axis ∥ [001]	CEF z-axis ∥ [110]	CEF z-axis ∥ [110]
	(a) Pr_2NiO_4			
2	0	−0.129	0.064	0.105
2	2		−0.112	(−0.051, 0.078)
4	0	−0.021	0.005	0.001
4	2		0.023	(0.015, −0.009)
4	4	−0.018	−0.013	(−0.008, −0.042)
6	0	−0.007	0.006	0.006
6	2		−0.004	(−0.005, 0.000)
6	4	0.008	−0.003	(−0.005, 0.001)
6	6		−0.007	(−0.007, −0.004)
	(b) Nd_2NiO_4			
2	0	−0.118	0.059	0.104
2	2		−0.102	(−0.036, 0.084)
4	0	−0.018	0.005	0.001
4	2		0.021	(0.012, −0.009)
4	4	−0.016	−0.011	(−0.007, −0.045)
6	0	−0.007	0.006	0.006
6	2		−0.005	(−0.005, 0.000)
6	4	0.009	−0.004	(−0.005, 0.002)
6	6		−0.007	(−0.007, −0.004)

[a] The relationship between the crystal-field Hamiltonian and the coordination factors is described by Hutchings [22]. The coefficients B_k^q of the Stevens operators O_q^k are related to the coordination factors by $B_k^q = -14.4 K_{kq} \theta_k \langle r^k \rangle \gamma_{kq}$ eV. The K_{kq} are numerical constants given by the expressions in front of the square brackets in table IV of Hutchings [22], and the θ_k are the reduced-matrix elements (α_J, β_J, γ_J) listed in table VI of Hutchings [22] for each trivalent lanthanide ion. $\langle r^k \rangle$ is the kth radial moment (in units of Å^k) of the 4f electron distribution [23]. The conversion factors relating the tensor operator coefficients B_q^k, defined in equation (3), to the Stevens operator coefficients B_k^q are given by Kassman [24].

on *relative changes* in the CEF; an *absolute* calculation would need to include the effects of further neighbours, screening, and bond delocalization.

Table 1 lists the point charge model coordination factors γ_{kq} (as defined by Hutchings [22]) for these geometries, calculated with a charge of $-2e$ on each oxygen ion. These factors have been given with respect to two different sets of Cartesian axes because the natural axes for describing the local crystal field are not always parallel to the crystallographic axes. For the distorted structure the natural direction for the CEF z-axis

is parallel to the normal of the mirror plane, i.e. the crystallographic [110] direction in the low-temperature tetragonal phase, whereas in the undistorted geometry it is simpler to choose the CEF z-axis to be parallel to the tetragonal axis, i.e. [001]. For the cases where the CEF z-axis ∥ [110] we have chosen the CEF x-axis ∥ [00$\bar{1}$]. This results in 15 non-zero γ_{kq} for the distorted structure (even q only). Since only 14 of these are independent it is always possible to eliminate one of them by a rotation of the CEF axes about the CEF z-axis.

Figures 8(a) and 8(b) are energy level diagrams for Pr^{3+} and Nd^{3+} respectively showing how the crystal-field splitting changes when the point symmetry is reduced from $4mm$ to m, according to the point charge model. The first excited state in both of the Pr^{3+} spectra is only slightly higher in energy than the ground state, and in the undistorted structure the wavefunctions for these two levels are almost purely of the form $(|m_J = +4\rangle \pm |m_J = -4\rangle)/\sqrt{2}$ (referred to the tetragonal CEF axes). The transition matrix element connecting these two singlets is by far the largest of all of the ground-state transitions. Similarly, in the undistorted Nd^{3+} spectrum the ground-state wavefunction is almost entirely comprised of $|+9/2\rangle$ and $|-9/2\rangle$ states, and the transition matrix element within the ground-state doublet is larger than the transition matrix elements joining the ground state to any of the other doublets. The distortion does not significantly change the transition probabilities.

The monoclinic distortion does cause shifts, typically of order 25%, in the energies of compatible levels, but the ordering of the levels, at lower energies in particular, is mostly preserved. We conclude, therefore, that the $4mm$ point symmetry is a useful first approximation for the crystal field at the R^{3+} site.

5. Determining the crystal field

As input to our fitting program we can specify the CEF energy levels of the R^{3+} ions relative to the ground state, the transition intensity ratios, and the size of any statically aligned magnetic moment. Each observable is weighted according to the experimental uncertainty.

The Nd^{3+} doublet energy levels and relative intensities of the $J = 9/2$ multiplet are determined directly from the neutron spectrum shown in figure 3. The heat capacity of Nd_2NiO_4, however, shows a maximum centred near 7 K (figure 5(b)) which cannot be attributed to one of the CEF levels. We interpret this anomaly as evidence for a splitting of the Nd^{3+} ground-state doublet in the molecular field from the Ni sublattice. A similar effect was encountered for Nd_2CuO_4 [9]. The Schottky anomaly corresponds to a splitting of 1.5 meV which, together with the other observed CEF doublet energies, gives a good description of the Nd^{3+} contribution to the heat capacity, as shown in figure 5(b).

Information on the Pr^{3+} CEF levels is less easily extracted from the data. As discussed above, the neutron spectra show a CEF level at 4.3 meV, and indicate at least two levels in the range 30–55 meV. Transitions to the remaining levels were not observed by neutron scattering, and so their location had to be estimated from the Pr_2NiO_4 heat capacity data. We fitted the measured ΔC_p to the Schottky contribution from the nine Pr^{3+} singlet levels, fixing levels at 0, 4.3, 40 and 47 meV, as suggested by the neutron spectra, and allowing the energies of the five remaining levels to vary. We were able to deduce with reasonable confidence from the ΔC_p data between 0 and 100 K that two levels must exist in the energy range 16–24 meV, and that the remaining levels lie above 40 meV. The overall splitting is unlikely to exceed 90 meV, given the observed splitting of the Nd^{3+} multiplet. The Pr^{3+} heat capacity calculated from both the directly and indirectly observed energy levels

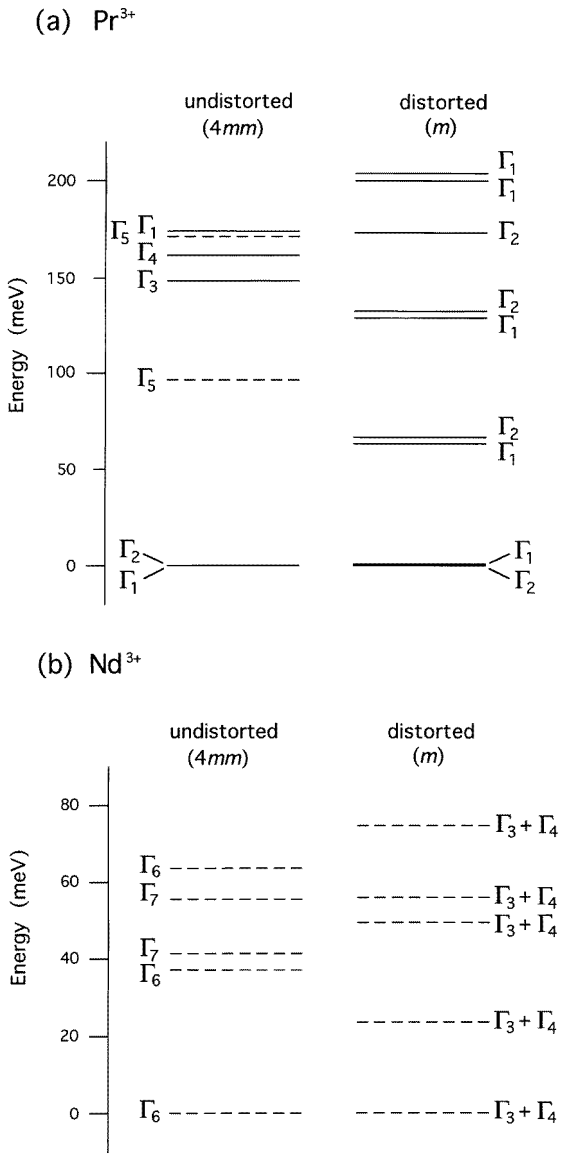

Figure 8. Results of the point charge model calculation of the energy levels of (a) Pr^{3+} and (b) Nd^{3+} in R_2NiO_4. The two diagrams correspond to the undistorted and distorted local environments illustrated in figure 7. Broken lines indicate doublet levels. The energy scale is only approximate since screening effects and the contributions to the electric field from more distant neighbours have been neglected.

is shown as the line in figure 5(a). The measured excess heat capacity above 60 K cannot be accounted for by the Pr^{3+} contribution, and is likely to be either a magnetic contribution from the Ni sublattice or a difference in the lattice estimate.

In table 2 we have collected together all the information about the Pr^{3+} and Nd^{3+} CEF excitations deduced from the neutron scattering and heat capacity data. The integrated intensities have been corrected for the $|\boldsymbol{Q}|$-dependence of the dipole form factor.

Table 2. Observed and calculated crystal-field transitions within the ground-state multiplet of (a) Pr_2NiO_4 and (b) Nd_2NiO_4. Transitions to the levels joined by brackets were unresolved. The intensities are given relative to the intensity of the strongest measured transition (=100). The calculated values correspond to the best-fit crystal-field parameters given in table 3—see later. I_{calc} is evaluated at the temperature of the measurement (45 K for Pr_2NiO_4 and 2 K for Nd_2NiO_4), and includes the contributions from transitions out of thermally populated levels above the ground state.

Level			Point group $4mm$			Point group m		
j	E_{obs}[a]	I_{obs}[b]	Γ_j[c]	E_{calc}	I_{calc}	Γ_j[c]	E_{calc}	I_{calc}
	(a) Pr_2NiO_4							
0	0.0		Γ_1	0.0	0	Γ_1	0.0	0
1	4.3 ± 0.2	100	Γ_2	3.7	100	Γ_2	3.3	100
2	16 ± 3	4 ± 2	Γ_4	42.3		Γ_1	18.2	6
3	24 ± 3		Γ_5	47.4		Γ_2	20.5	
4	40 ± 4	30 ± 5		47.4		Γ_1	38.3	35
5	47 ± 4		Γ_3	51.3	55	Γ_2	44.8	
6	51 ± 5		Γ_1	60.9		Γ_1	54.3	
7	63 ± 10	9 ± 5	Γ_5	71.3		Γ_2	54.7	8
8	75 ± 10			71.3		Γ_1	78.9	
	(b) Nd_2NiO_4							
0	0.0[d]		Γ_6	0.0	0	$\Gamma_3 + \Gamma_4$	0.0	0
1								
2	7.1 ± 0.5	50 ± 8	Γ_6	9.5	41	$\Gamma_3 + \Gamma_4$	7.0	45
3								
4	22.5 ± 0.5	100	Γ_6	23.0	100	$\Gamma_3 + \Gamma_4$	22.3	100
5								
6	37.0 ± 1	100 ± 6	Γ_7	28.3	97	$\Gamma_3 + \Gamma_4$	38.9	107
7								
8	48.5 ± 1	50 ± 10	Γ_7	55.3	59	$\Gamma_3 + \Gamma_4$	48.9	47
9								

[a] For Pr_2NiO_4, the only excited levels observed directly in the neutron spectra are those at 4.3, 40 and 47 meV. From the heat capacity data we deduce the existence of two levels between 16 meV and 24 meV, and conclude that the remaining levels are above 50 meV. The errors assigned to the energies not directly observed are confidence indicators used as statistical weights in the evaluation of χ^2.

[b] The observed relative intensities were estimated from the areas under the peaks in the experimental neutron spectra corrected for the form factors, of Pr^{3+} and Nd^{3+}. The errors attached to the values reflect the uncertainty in this procedure.

[c] Γ_j is the irreducible representation according to which the wavefunction transforms under the symmetry operations of the point group. The convention of Koster *et al* [25] has been followed.

[d] The ground-state doublet of Nd_2NiO_4 is split by 1.5 meV at low temperature (deduced from the 7 K anomaly in the heat capacity).

5.1. The tetragonal approximation

Following the conclusions of our point charge model analysis, we attempted firstly to find the set of five tetragonal intrinsic CEF parameters (A_0^2, A_0^4, A_4^4, A_0^6, A_4^6) which gave the best simultaneous description of the experimental data for both compounds. As well as approximating the local site symmetry to $4mm$, this procedure assumes that the factorization given in equation (4) is valid and that both ions experience the same intrinsic crystal field. The advantage of this approach is that it gives us more observables per parameter than if

each compound were analysed separately, and thereby increases the chances of finding a unique set of parameters. We cannot expect to obtain a perfect match, though, because in reality these assumptions are only approximately valid.

We varied the crystal-field parameters by a standard, least-squares fitting algorithm which aims to achieve the best agreement between the observed and calculated data through minimization of the χ^2-parameter. In order to cover a wide range of parameter space we executed the fit for the 32 combinations of starting parameters generated by assigning to each of the B_q^k either the value $+100$ meV or -100 meV.

Table 3. Crystal-field parameters in tensor notation (equation (3)), and in units of meV, obtained from simultaneous fits to the neutron scattering spectra for Pr_2NiO_4 and Nd_2NiO_4. The different axes are the same as in table 1. The parameters correspond to Pr^{3+}, but those for Nd^{3+} can be obtained by the scaling procedure described in the text. Complex crystal-field parameters are given in brackets as $(B^{(c)k}_q,\ B^{(s)k}_q)$. Otherwise the parameter is real, and the value given is $B^{(c)k}_q$.

		Undistorted (4*mm*)		Distorted (*m*)
k	q	CEF z-axis ∥ [001]	CEF z-axis ∥ [110]	CEF z-axis ∥ [110]
2	0	79 ± 10	-40	-77
2	2		49	45[b]
4	0	160 ± 18	27	18
4	2		-84	$(-37, -57)$
4	4	32 (-32)[a] ± 9	80	$(-29, -57)$
6	0	-181 ± 17	-7	29
6	2		-42	(8, 74)
6	4	-91 $(+91)$[a] ± 8	137	(54, -114)
6	6		-63	$(-40, 15)$

[a] A simultaneous change of signs of $B^{(c)4}_4$ and $B^{(c)6}_4$ leads to the same calculated spectrum in tetragonal symmetry. If the signs are reversed then the fourth- and sixth-order parameters in the case of the CEF z-axis ∥ [110] (second column) will be different to those given above. Physically, the sign reversal corresponds to a 45° rotation of the CEF axes about the z-axis.

[b] We have chosen $B^{(s)2}_2$ to be zero to restrict the number of parameters to 14, the minimum number required to describe a crystal field of symmetry *m*.

We found only one set of fitted parameters which agreed well with the observed transition energies and relative intensities, and these parameters are listed in table 3. The energies and intensities calculated from the best-fit parameters are given in table 2 beside the observed data. The lowest two Pr^{3+} wavefunctions are of Γ_1 and Γ_2 symmetry respectively, and the ground state of Nd^{3+} is Γ_6.

Although a satisfactory description of the data in terms of just the five tetragonal CEF parameters has been found, the tetragonal model is still only a first approximation. The energies of some of the fitted CEF levels differ significantly from their known positions, and from a comparison of the point charge model calculations for the 4*mm* and *m* symmetries (figures 8) we must expect the energy levels to be in error by typically 25%. Further, the size of the ordered moment on the Nd^{3+} ion predicted (1.3 μ_B) is much less than the experimental value of 3.2 μ_B[1], and even when we included the Nd^{3+} ordered moment as an observable in the fit we were not able to increase it without compromising the agreement with the other data. In the second stage of the analysis, therefore, we attempted to fit the data with the full set of 14 independent CEF parameters allowed by symmetry.

5.2. Full monoclinic site symmetry

The possibility of such a fit would appear marginal in view of the large number of undetermined parameters. We do nevertheless have in excess of 14 observables (the data in tables 2 together with the Nd^{3+} low-temperature ordered moment), even though some of them are rather loosely constrained.

Table 4. Wavefunctions of the lowest two CEF energy levels of (a) Pr^{3+} and (b) Nd^{3+} in R_2NiO_4 calculated from the CEF parameters (without a molecular field) given in table 3 for the m point symmetry. The wavefunctions refer to the set of axes with the CEF z-axis parallel to the crystallographic [110]. The corresponding calculated transitions are given in table 2. The table entries are the coefficients of the states $|m_J\rangle$ in the linear expansion of the wavefunctions $|\Gamma_j\rangle$. Small contributions to the $|\Gamma_j\rangle$ from J-multiplets other than the ground state are not listed.

(a) Pr_2NiO_4

Γ_j	E_{calc} (meV)	−4	−3	−2	−1	0	+1	+2	+3	+4
Γ_1	0.0	−0.117 − 0.012i	—	0.415 + 0.216i	—	0.726	—	0.415 − 0.216i	—	−0.117 + 0.012i
Γ_2	3.3	—	0.134 + 0.155i	—	0.609 + 0.286i	—	0.672	—	0.187 − 0.084i	—

(b) Nd_2NiO_4

Γ_j	E_{calc} (meV)	−9/2	−7/2	−5/2	−3/2	−1/2	+1/2	+3/2	+5/2	+7/2	+9/2
$(\Gamma_3+\Gamma_4)$	0.0	0.144 + 0.336i	—	0.067 − 0.097i	—	0.699	—	0.314 + 0.450i	—	0.135 − 0.189i	—
		—	0.135 + 0.189i	—	0.314 − 0.450i	—	0.699	—	0.067 + 0.097i	—	0.144 − 0.336i
$(\Gamma_3+\Gamma_4)$	7.0	0.383 − 0.127i	—	0.580	—	0.054 − 0.326i	—	−0.475 + 0.268i	—	−0.094 + 0.272i	—
		—	−0.094 − 0.272i	—	−0.475 − 0.268i	—	0.054 + 0.326i	—	0.580	—	0.383 + 0.127i

With the five CEF parameters from the tetragonal fit (rotated so that the CEF z-axis ∥ [110]) as starting parameters, and the constraint $B^{(s)}_2{}^2 = 0$ to restrict the number of parameters to 14, we found several parameter sets that gave a good description of the data ($\chi^2 < 10$). Inspection of the wavefunctions, however, revealed that these fits were variations of essentially the same solution, and given the limited experimental data we could not realistically discriminate between them further. In table 3 we give the parameter set for the best of the fits ($\chi^2 = 2.7$), and in table 4 we give the corresponding wavefunctions for the lowest two CEF energy levels. Note that although the CEF z-axis is parallel to [110], the orientation of the CEF x- and y-axes relative to the crystal structure is undetermined at this stage, and will be discussed later.

The energies and intensities calculated from the monoclinic fit are given in table 2, together with the symmetries of the wavefunctions. In figure 9 we show the scattering function $S(\boldsymbol{Q}, \omega)$ calculated from equation (2) with the same temperatures as applied to the experimental neutron spectra. As is to be expected, the increased number of fitting parameters leads to a better match to the experimental data than could be obtained with just the tetragonal parameters. In addition, the ground-state magnetic moment on the Nd^{3+} is now 2.5 μ_B, much closer to the observed value. At the same time, one can see in table 3

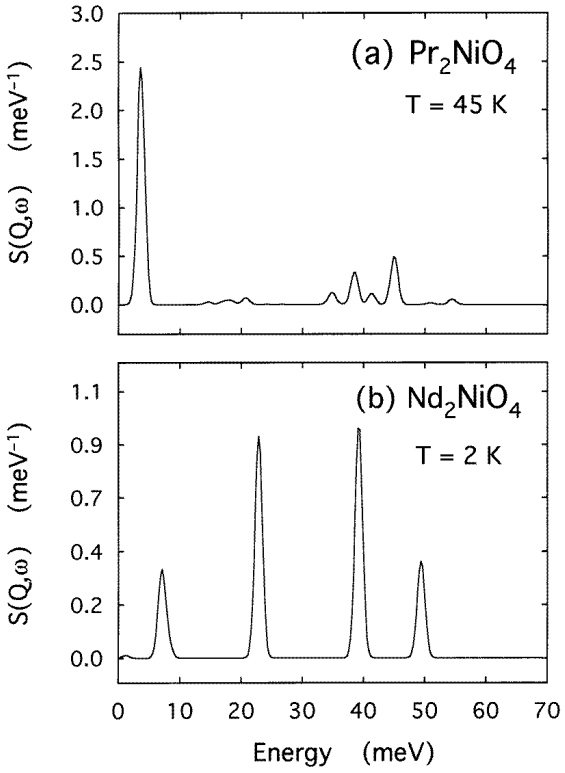

Figure 9. The scattering functions $S(\boldsymbol{Q}, \omega)$ calculated from equation (2) with the monoclinic crystal-field model. The functions are evaluated at the same temperatures as were used in the neutron experiments. Apart from a weak $\boldsymbol{Q}$-dependence from the form factors (see equation (1)) the functions $S(\boldsymbol{Q}, \omega)$ simulate the R^{3+} contributions to the spectra in figures 1 and 3.

that the moduli of the monoclinic CEF parameters are not dissimilar from those of the tetragonal set, and this confirms that the monoclinic fit is essentially a refinement of the tetragonal model.

In figures 6(a) and 6(b) we have included the calculated magnetic susceptibilities for the monoclinic fit for Pr_2NiO_4 and Nd_2NiO_4 respectively. Above $\sim$130 K the measured and calculated susceptibilities are in near agreement for both compounds, and are close to the free-ion Curie susceptibilities for Pr^{3+} ($J = 4$) and Nd^{3+} ($J = 9/2$). At lower temperatures, where reorientations in the Ni^{2+} sublattice ordering and cooperative effects in the R^{3+} sublattice are responsible for the most significant features, the calculated susceptibilities differ greatly from the measurements. This is because the calculations only include the R^{3+} single-ion contribution to the susceptibility.

6. Discussion

We have thus far presented a model for the monoclinic crystal field at the R^{3+} site in R_2NiO_4 which gives a good description of the inelastic neutron scattering, specific heat capacity and susceptibility data of both compounds. As things stand, however, we cannot make full use of the results because the relationship between the crystal-field axes, to which

the wavefunctions in tables 4 refer, and the crystallographic axes is not yet completely established. We know that the crystal-field z-axis is parallel to the normal of the mirror plane (the crystallographic [110] direction), but the orientation within the mirror plane of the crystal-field x- and y-axes is still undetermined.

We will attempt to resolve this uncertainty by considering the directions of the R^{3+} ordered magnetic moments at low temperature. The neutron diffraction investigation of Rodríguez-Carvajal *et al* [1] on Nd_2NiO_4 showed that both the Ni and Nd sublattices are ordered antiferromagnetically at 1.5 K, with the Nd^{3+} moments of magnitude 3.2 μ_B inclined at an angle of 19° to the crystallographic ab-plane. A similar behaviour was found in Pr_2NiO_4 [2, 16] except that the Pr sublattice is only partially ordered at 1.5 K, with a moment of magnitude 1.1–1.3 μ_B inclined at an angle 36–42° away from the ab-plane induced on the Pr^{3+} ions through coupling to the Ni sublattice.

Table 5. The wavefunctions of table 4 rotated so that the CEF z-axis is approximately parallel to the crystallographic [001] direction. The CEF x-axis lies in the mirror plane, and the CEF y-axis is normal to the mirror plane (parallel to the crystallographic [110] direction).

(a) Pr_2NiO_4

Γ_j	E_{calc} (meV)	−4	−3	−2	−1	0	+1	+2	+3	+4
Γ_1	0.0	0.375	0.470	0.252	0.076	0.361	−0.076	0.252	−0.470	0.375
Γ_2	3.3	0.367	0.419	0.315	0.291	—	0.291	−0.315	0.419	−0.367

(b) Nd_2NiO_4

Γ_j	E_{calc} (meV)	−9/2	−7/2	−5/2	−3/2	−1/2	+1/2	+3/2	+5/2	+7/2	+9/2
$(\Gamma_3+\Gamma_4)$	0.0	0.048	0.388	0.376	0.488	0.053	0.174	0.282	0.551	0.200	0.049
		0.049	−0.200	0.551	−0.282	0.174	−0.053	0.488	−0.376	0.388	−0.048
$(\Gamma_3+\Gamma_4)$	7.0	0.654	0.280	0.024	−0.172	−0.443	−0.357	0.163	−0.016	−0.135	0.289
		−0.289	−0.135	0.016	0.163	0.357	−0.443	0.172	0.024	−0.280	0.654

In the monoclinic crystal-field model the Nd^{3+} ordered moment (2.5 μ_B) lies in the CEF xy-plane, rotated at an angle of 25° away from the CEF x-axis towards $-y$. Moreover, the single-ion anisotropy is very large, and the moment direction is relatively insensitive to the presence of a small molecular field $\boldsymbol{B}_{mf}$, so long as there is some component of $\boldsymbol{B}_{mf}$ along the CEF x-axis. For Pr_2NiO_4 the ordered moment is zero in the singlet ground state, but a moment can be induced by a molecular field. Again, the anisotropy is large, and the induced moment aligns at an angle of 13° from the CEF x-axis towards $+y$ almost irrespective of the direction of $\boldsymbol{B}_{mf}$. According to our model, therefore, the CEF x-axis lies in between the directions of the ordered Nd^{3+} and Pr^{3+} moments, closest to the latter. With this information we can now line up the observed and predicted moment directions, and hence deduce the relative orientations of the CEF and crystallographic axes. The best alignment is found when the CEF x-axis is at an angle of approximately 30° to the crystallographic ab-plane, and lies in the mirror plane. Having established this relationship we can now rotate the axes and refer the CEF wavefunctions to the crystallographic axes. The results are given in tables 5.

Batlle *et al* [17] have estimated a value of 5.2 ± 0.6 T for the component of $\boldsymbol{B}_{mf}$ parallel to the crystallographic z-direction based on a mean-field theory analysis of their magnetization data on Nd_2NiO_4. According to our monoclinic crystal-field model a

molecular field of magnitude 5.2 T applied parallel to the crystallographic z-axis splits the Nd^{3+} ground-state doublet by 1.3 meV and induces a moment of 0.5 μ_B on the Pr ions. The splitting extracted from the C_p Schottky anomaly is 1.5 meV, and the observed Pr^{3+} ordered moment at 1.5 K is $\sim$1.2 μ_B [2, 16]. By adjusting the magnitude and direction of $\boldsymbol{B}_{mf}$ we could make the calculated splitting and induced moment agree more closely with the experimental values, but such refinement is not helpful as the real direction of $\boldsymbol{B}_{mf}$ is not known and may be different in the two compounds. Nevertheless, these calculations do at least demonstrate that a 5.2 T molecular field is not unreasonable. We also calculate that a field of this magnitude would not significantly perturb the CEF energy levels of Pr_2NiO_4, and would cause a splitting of the other doublets in Nd_2NiO_4 by no more than 1.3 meV. This suggests that the peak broadening observed in the neutron spectrum of Nd_2NiO_4 is not due to doublet splitting, and is more likely to be a result of local strain or oxygen non-stoichiometry.

Table 6. Wavefunctions for the lowest two CEF energy levels of (a) Pr^{3+} and (b) Nd^{3+} in R_2CuO_4 calculated from the CEF parameters given in reference [10], in the absence of a molecular field. Small contributions to the $|\Gamma_j\rangle$ from J-multiplets other than the ground state are not listed.

(a) Pr_2NiO_4

Γ_j	E_{calc} (meV)	−4	−3	−2	−1	0	+1	+2	+3	+4
Γ_3	0.0	—	—	0.706	—	—	—	0.706	—	—
Γ_5	18.2	—	0.855	—	0.001	—	0.509	—	—	—
		—	—	—	0.509	—	−0.001	—	0.855	—

(b) Nd_2NiO_4

Γ_j	E_{calc} (meV)	−9/2	−7/2	−5/2	−3/2	−1/2	+1/2	+3/2	+5/2	+7/2	+9/2
Γ_6	0.0	0.531	—	—	—	0.645	—	—	—	0.542	—
		—	0.542	—	—	—	0.645	—	—	—	0.531
Γ_7	14.6	—	—	0.929	—	—	—	−0.355	—	—	—
		—	—	—	−0.355	—	—	—	0.929	—	—

Finally, it is of interest to compare the wavefunctions for the R^{3+} ions in R_2NiO_4 (R = Pr, Nd) with those of R^{3+} in R_2CuO_4. This is most easily accomplished if the CEF quantization axis is the same for both compounds. In the cuprates the symmetry of the R^{3+} site is not distorted, and so the tetragonal point group $4mm$ (not $4/mmm$ as given in reference [10]) describes the CEF exactly. Hence, it is natural to use an axis system with the CEF z-axis parallel to the crystallographic [001]. Accordingly, the wavefunctions from our model for the crystal field in R_2CuO_4 (R = Pr, Nd) [10] have been listed in table 6, and these may be compared with the nickelate wavefunctions listed in table 5 (for which the CEF z-axis is approximately parallel to the crystallographic [001]). It can be seen from table 6 that the ground state of Pr^{3+} in Pr_2CuO_4 is almost pure $\Gamma_3 = (|+2\rangle + |-2\rangle)/\sqrt{2}$, while the ground-state doublet of Nd^{3+} in Nd_2CuO_4 is $\Gamma_6 = 0.531|\pm 9/2\rangle + 0.542|\pm 7/2\rangle + 0.645|\pm 1/2\rangle$. These are quite different from the ground states of R^{3+} in the nickelates, and these differences must be taken into consideration in any comparison of the physical properties of the cuprates and nickelates.

7. Conclusions

The tetragonal approximation to the crystal field at the R^{3+} site is useful in that it allows us to locate the general position in the space of the five tetragonal crystal-field parameters. It reproduces most of the experimental results, but there are significant discrepancies which cannot be refined. Using the tetragonal approximation as a starting point we have analysed the experimental data in rather great detail in terms of a crystal-field model with the actual monoclinic site symmetry.

The low-temperature physical properties of the Pr^{3+} ions in Pr_2NiO_4 arise almost entirely from two singlets separated in energy by 4.3 meV, and of Γ_1 and Γ_2 symmetry respectively. The ground-state doublet of Nd^{3+} in Nd_2NiO_4 is separated from the first excited doublet by 7.1 meV. Symmetry requires that the crystal-field quantization (z-) axis is parallel to the crystallographic [110] direction, and our analysis suggests that the crystal-field x-axis lies in the mirror plane at an angle of approximately 30° to the crystallographic ab-plane. We list the low-energy wavefunctions in tables 4 and 5, the latter compilation being referred to a set of axes conveniently related to the crystallographic axes to facilitate their use in practical applications.

While we acknowledge that the model could be subject to further refinement in the future, when more data become available, we nevertheless believe that the present description captures the essential physics behind the magnetic behaviour of R^{3+} ions in R_2NiO_4.

Acknowledgments

One of us (ATB) thanks the Physics Department at Risø National Laboratory for its hospitality and financial support, and for making available computing facilities during a three-month visit when much of the analysis presented here was performed. We acknowledge the support of the EPSRC for a Studentship (AL) and for provision of neutron facilities at ISIS. Financial support from CICYT, project number MAT94-0804, is also acknowledged.

References

[1] Rodríguez-Carvajal J, Fernández-Díaz M T, Martínez J L, Fernández F and Saez-Puche R 1990 *Europhys. Lett.* **11** 261
[2] Fernández-Díaz M T, Rodríguez-Carvajal J, Martínez J L, Fillion G, Fernández F and Saez-Puche R 1991 *Z. Phys.* B **82** 275
[3] Rodríguez-Carvajal J, Martínez J L, Pannetier J and Saez-Puche R 1988 *Phys. Rev.* B **38** 7148
[4] Lander G H, Brown P J, Spalek J and Honig J M 1989 *Phys. Rev.* B **40** 4463
[5] Gopalakrishnan J, Colsman G and Reuter B 1977 *J. Solid State Chem.* **22** 145
[6] Doyle S M, Sridhar Kumar M P and Paul D McK 1992 *J. Phys.: Condens. Matter* **4** 3559
[7] Tokura Y, Takagi H and Uchida S 1989 *Nature* **337** 345
[8] Brugger T, Schreiner T, Roth G, Adelmann P and Czjzek G 1993 *Phys. Rev. Lett.* **71** 2481
[9] Boothroyd A T, Doyle S M, Paul D McK, Misra D S and Osborn R 1990 *Physica* C **165** 17
[10] Boothroyd A T, Doyle S M, Paul D McK and Osborn R 1992 *Phys. Rev.* B **45** 10 075
[11] Lovesey S W 1984 *Theory of Neutron Scattering from Condensed Matter* vol 2 (Oxford: Oxford University Press)
[12] Taylor A D, Boland B C, Bowden Z A and Jones T J L 1987 *Rutherford Appleton Laboratory Internal Report* RAL-87-012
[13] Boothroyd A T, Doyle S M, Sridhar Kumar M P, Paul D McK and Osborn R 1990 *J. Less-Common Met.* **164+165** 915
[14] Castro M and Burriel R 1995 *Thermochim. Acta* **269+270** 523

Castro M and Burriel R 1995 *Thermochim. Acta* **269+270** 537
[15] Pintschovius L, Bassat J M, Odier P, Gervais F, Chevrier G, Reichardt W and Gompf F 1989 *Phys. Rev.* B **40** 2229
[16] Fernández-Díaz M T, Martínez J L, Rodríguez-Carvajal J, Beille J, Martínez B, Obradors X and Odier P 1993 *Phys. Rev.* B **47** 5834
[17] Batlle X, Obradors X and Martínez B 1992 *Phys. Rev.* B **45** 2830
[18] Saez Puche R, Fernández F, Rodríguez-Carvajal J and Martínez J L 1989 *Solid State Commun.* **72** 273
[19] Boothroyd A T, Doyle S M and Osborn R 1993 *Physica* C **217** 425
[20] Carnall W T, Goodman G L, Rajnak K and Rana S 1989 *J. Chem. Phys.* **90** 3443
[21] Walter U 1984 *J. Phys. Chem. Solids* **45** 401
[22] Hutchings M T 1964 *Solid State Physics* vol 16 (New York: Academic) p 227
[23] Freeman A J and Watson R E 1962 *Phys. Rev.* **127** 2058
[24] Kassman A J 1970 *J. Chem. Phys.* **53** 4118
[25] Koster G F, Dimmock J O, Wheeler R G and Statz H 1963 *Properties of the Thirty-Two Point Groups* (Cambridge, MA: MIT Press)